Three-dimensional multiple optical cages formed by focusing double-ring shaped radially and azimuthally polarized beams

Tingting Zeng (曾婷婷) and Jianping Ding (丁剑平)*

National Laboratory of Solid Microstructure and School of Physics, Nanjing University, Nanjing 210093, China
**Corresponding author: jpding@nju.edu.cn*

Received October 11, 2017; accepted January 12, 2018; posted online March 6, 2018

We propose and simulate a method for generating a three-dimensional (3D) optical cage in the vicinity of focus by focusing a double-ring shaped radially and azimuthally polarized beam. Our study shows that the combination of an inner ring with an azimuthally polarized field and an outer ring with a radially polarized field and a phase factor can produce an optical cage with a dark region enclosed by higher intensity. The shape of the cage can be tailored by appropriately adjusting the parameters of double-mode beams. Furthermore, multiple 3D optical cages can be realized by applying the shift theorem of the Fourier transform and macro-pixel sampling algorithm to a double-ring shaped radially and azimuthally polarized beam.

OCIS codes: 050.1960, 260.5430, 140.3300.
doi: 10.3788/COL201816.031405.

Optical cage is a specific kind of optical field that has a dark region surrounded by higher intensity. Owing to its intriguing distribution, an optical cage can be applicable to a multitude of areas, such as optical trapping and manipulation[1–6] and optical imaging[7–9]. Consequently, the generation of an optical cage has attracted much attention from researchers. Kozawa and Sato generated an optical cage from a double-ring radially polarized beam[10]. Chen and Cai produced a controllable optical cage by focusing a Laguerre-Gaussian correlated Schell-mode beam[11]. The above two techniques can produce only nonuniform optical cages. To improve the uniformity of the optical cage, Zhang applied a helical phase plate onto double-ring radially polarized beams[12]. Bokor and Davidson used two counter-propagating radially polarized Laguerre-Gaussian beams to realize a hollow dark spherical spot enclosed by relatively uniform optical barrier[13], but this method required a sophisticated focusing system and elaborate optical alignment. Wang *et al.* proposed to modulate the polarization state of the incident beam to produce a uniform optical cage in the focused field[14]. However, all of the researches mentioned above are limited to a single optical cage. Guo *et al.* designed a complex pupil filter for the incident Laguerre-Gaussian beams to realize multiple optical cages along the optical axis[15]. Weng *et al.* proposed a polarization steering method for generating multiple optical cages either in the transverse plane[16] or along the optical axis[17]. Naturally, the generation of a three-dimensional (3D) array of optical cages with arbitrary spacing between them becomes appealing but still remains a challenge to date. In this work, we present a method to generate a 3D optical cage array with good uniformity in the vicinity of focus from vector beams carrying radial and azimuthal polarizations, respectively, in their two concentric zones of cross-section. The proposed scheme is capable of tailoring the shape of cages, as well as the structure of multiple cages, and is validated by numerical simulation.

Our work is first focused on how to combine the radial and azimuthal polarizations in double-ring modes of incident light to produce a dark focal region surrounded with uniform optical barriers. Then, we explore the possibility of tailoring the intensity distribution at the vicinity of the focus by appropriately adjusting the parameters of the double-ring mode and the axial shifting factor. Finally, we apply the shift theorem of Fourier transform and the macro-pixel sampling algorithm to a double-ring shaped radially and azimuthally polarized beam with the aim at generating multiple 3D optical cages.

It is known that tightly focusing an azimuthally polarized beam can create a dark field at the focus with higher intensity in the transverse direction than in the axial direction[18]. In contrast, focusing a radially polarized beam can produce a strong longitudinal electric field along the optical axis[19]. Our idea is to purposely split the field contributed from the radially polarized part of incident double-ring-mode light along the axial direction so that it combines with the contribution of the azimuthally polarized part to yield a 3D dark focus. To accomplish this, we impose on the radially polarized part a phase modulation factor expressed by

$$T_1 = \exp\{i\,\mathrm{angle}[\exp(ik_z z_d) + \exp(-ik_z z_d)]\}, \qquad (1)$$

where angle means to take the argument of the complex function, and k_z is the z-directional component of the wave vector. According to the shift theorem of Fourier transform, this phase factor will induce double axial shifts of z_d and z_d in the far-field space (or focal volume).

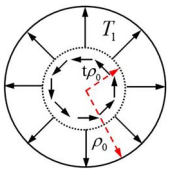

Fig. 1. Polarization state of the double-mode vector beam.

Figure 1 is the polarization distribution pattern of a double-mode vector beam. The electric field of this incident beam can be expressed in a Cartesian coordinate system as

$$\vec{E}_{\text{in}}(x,y,z)=\begin{cases} T_1\vec{E}_r & t\rho_0 < r \le \rho_0 \\ \vec{E}_\varphi & 0 \le r \le t\rho_0 \end{cases}, \tag{2}$$

where $\vec{E}_r$ and $\vec{E}_\varphi$ represent the radial and azimuthal polarized field in the input plane, respectively, ρ_0 is the beam's maximum radius that is determined by the entrance pupil of the objective lens used here, and t is the ratio of the inner mode to the outer mode in the radius.

The focusing process through an aplanatic lens is schematically illustrated in Fig. 2. The electric field $\vec{E}$ in the vicinity of focus can be calculated by the vectorial diffraction integral[20,21], which can be further simplified in the sense of the Fourier transform; the focal field at the point $(x,\ y,\ z)$ with respect to the focus can be expressed[21] as

$$\vec{E}(x,y,z)=\text{FT}\{\vec{E}_t(x,y,z)e^{ik_z z}/\cos\theta\}, \tag{3}$$

where a multiplicative constant factor has been dropped for clarification. $\vec{E}_t$ is the field in the exit aperture of the focusing lens. FT$\{\cdot\}$ denotes the two-dimensional (2D) Fourier transform. The exit field $\vec{E}_t$ in Eq. (3) can be expressed by the incident field $\vec{E}_{\text{in}}$ in the transformation form[22],

$$\vec{E}_t(x,y,z)=l_0(\theta)\sqrt{\cos\theta}\boldsymbol{M}\,T_2\vec{E}_{\text{in}}(x,y,z), \tag{4}$$

where $l_0(\theta)$ is the relative amplitude of the electric field of the incident beam at a pupil plane. $\boldsymbol{M}$ is the transformation matrix of the lens, taking the following form:

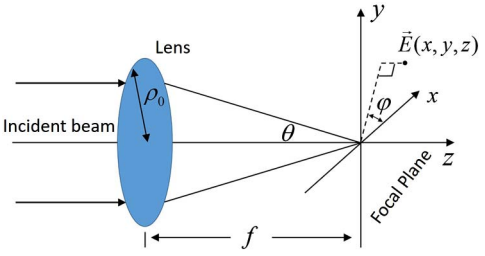

Fig. 2. Schematic of the focusing system.

$$\boldsymbol{M}=\begin{bmatrix} \cos^2\varphi\cos\theta+\sin^2\varphi & (\cos\theta-1)\sin\varphi\cos\varphi & -\sin\theta\cos\varphi \\ (\cos\theta-1)\sin\varphi\cos\varphi & \cos^2\varphi+\sin^2\varphi\cos\theta & -\sin\theta\sin\varphi \\ \sin\theta\cos\varphi & \sin\theta\sin\varphi & \cos\theta \end{bmatrix}. \tag{5}$$

In Eq. (4), T_2 is a specific phase factor needed to impose on the incident beam for generating multiple optical cages, which will be explained in detail later. For the single optical cage, we just set $T_2 = 1$.

In this Letter, the incident field profile is assumed to be Gaussian, and, hence, the relative amplitude can be expressed as

$$l_0(\theta)=\begin{cases} \exp[-\beta_0(\sin\theta/\sin\alpha)^2] & 0 \le r \le \rho_0 \\ 0 & \text{otherwise} \end{cases}, \tag{6}$$

where β_0 is the ratio of the pupil radius to the beam waist, and $\alpha=\arcsin(NA/n)$ is the maximum value of θ with n denoting the refractive index in the exit space and depends on the numerical aperture (NA) of the objective. In the following simulation, we will set $NA = 0.8$.

In the first simulation example, we choose $\beta_0 = 1.12$, $z_d = 3\lambda$ ($\lambda = 0.532$ μm denoting the wavelength of light), and $t = 0.6$. Figure 3 draws the calculated results of intensity distributions of each component. Since the focusing configuration has cylindrical symmetry, hereinafter, we plot only the distribution in the x-z plane, unless stated otherwise. For all of the calculations in this Letter, the length unit is normalized to wavelength λ. As shown in Fig. 3(a), the intensity of the transverse component $|E_r|^2+|E_\varphi|^2$ on the optical axis is null at any z position. However, it is noted in Fig. 3(b) that the longitudinal component gives rise to two symmetrical bright spots on the optical axis sandwiching a dark region. Figure 3(c) gives the total intensity distribution obtained by a summation of the distributions in Figs. 3(a) and 3(b). Figure 3(d) presents the normalized profile of total intensity along

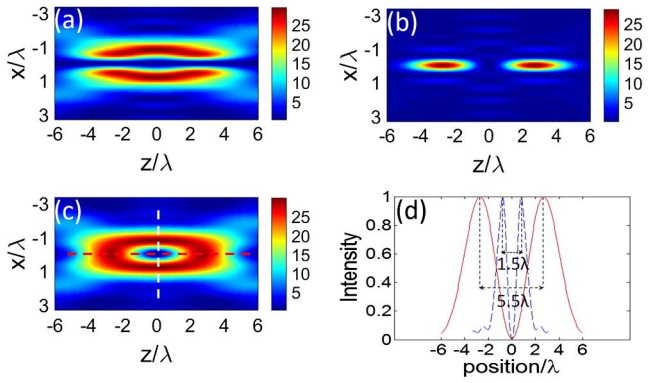

Fig. 3. Calculated intensity distributions of in the x-z plane with setting parameters $\beta_0 = 1.12$, $z_d = 3\lambda$, and $t = 0.6$. (a) Intensity of transverse component $|E_r|^2+|E_\varphi|^2$, (b) intensity of longitudinal component $|E_z|^2$, (c) total intensity distribution, (d) normalized intensity profile along the z and x axes [marked in (c) by the red and white dotted lines, respectively].

the z axis and x axis (marked respectively in Fig. 3(c) by the red and white dashed lines), where the red solid line and blue dotted line stand for the total intensity distribution along the z axis and x axis, respectively. They have the same maximum intensity and similar intensity distribution. Figure 3 shows that the optical cage surrounded uniformly by light in the transverse and longitudinal directions has been achieved by using our method. The size of the optical cage can be defined by the dimension of a bright barrier spanning along the transverse and axial directions. As shown in Fig. 3(d), the dimensions of 5.5λ along the z axis and of 1.5λ in the focal plane are obtained, respectively.

Then, we explore the tunability of the optical cage generated by our method. In fact, we will see in the following examples shown in Fig. 4 that the intensity distribution of the optical cage barrier can be accurately tuned by adjusting the parameters of the ratio t of the inner mode to the outer mode in the radius, the distance of axial shift z_d, and the ratio β_0 of the pupil radius to the beam waist.

Figure 4 shows the total intensity distributions in the x-z plane in the vicinity of focus for the incident beams with different parameters. The incident beams yielding Figs. 4(a) and 4(b) are the same in $\beta_0 = 1.12$, and $z_d = 3\lambda$, but differ in the radius of the inner and outer modes by setting $t = 0.3$, and $t = 0.8$, respectively. We can see that the increase of the ratio t (=inner-mode radius/outer-mode radius) gives rise to the higher optical barrier in the radial direction than in the axial direction. This phenomenon is ascribed to the fact that increasing the ratio t will enlarge the relative area of azimuthal polarization, which contributes more to the transverse

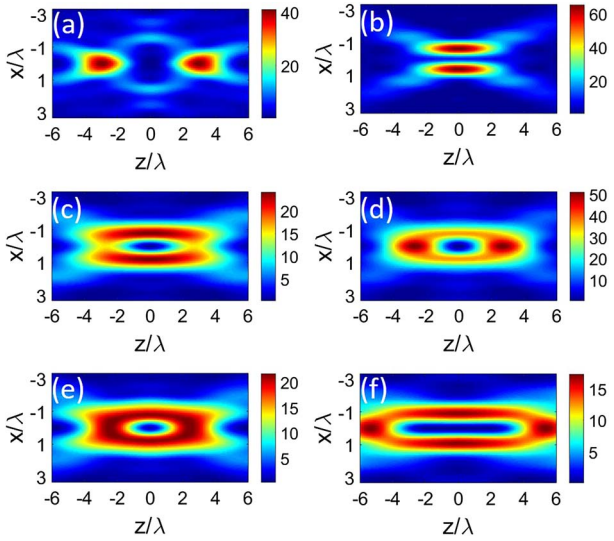

Fig. 4. Calculated intensity distributions with different parameters in the x-z plane. (a),(b) The same $z_d = 3\lambda$ and $\beta_0 = 1.12$, but different $t = 0.3$, and $t = 0.8$, respectively; (c),(d) The same $z_d = 3\lambda$, and $t = 0.6$, but different $\beta_0 = 1.6$, and $\beta_0 = 0.7$, respectively; (e),(f) The same $t = 0.55$, and $\beta_0 = 1.5$, but different $z_d = \lambda$, and $z_d = 5\lambda$, respectively.

component in the focal field. Figures 4(c) and 4(d) show the total intensity distributions with the same $z_d = 3\lambda$, and $t = 0.6$, but with different $\beta_0 = 1.6$, and $\beta_0 = 0.7$, respectively. This result indicates that the smaller the radius ratio β_0 between the pupil and beam waist, the higher the optical barrier in the axial direction than in the radial direction. This result is owing to the fact that the smaller β_0 is, the stronger the outer part of the incident field is relatively, giving rise to a stronger radial polarization of incident light. Figures 4(e) and 4(f) demonstrate the performance of adjusting the parameter z_d in the T_1 function. The focal intensity distributions with the depth of 4.2λ and 10.4λ are produced, respectively, for $z_d = 1\lambda$ and $z_d = 5\lambda$, with the same $t = 0.55$, and $\beta_0 = 1.5$. We can see that the increase of z_d enables the increasing depth of the optical cage, which is just due to the axial shifting role of z_d. The demonstration in Fig. 4 confirms that the intensity distribution of the optical cage can be flexibly configured by appropriately adjusting the parameters of double-mode incident beams.

Increasing the number of optical cages can further facilitate applications of such a special optical field. The 3D array of optical cages is of special interest to us. Here, in order to realize the 3D optical cage array, we again apply the shift theorem of Fourier transform to the above-discussed single-cage beams. For this purpose, let the phase factor T_2 take the following form:

$$T_2 = \exp[-i(k_x\Delta x + k_y\Delta y + k_z\Delta z)], \tag{7}$$

where Δx, Δy, and Δz are the desired shift distance of the focal spot in the x, y, and z directions, respectively. For creating an array with N cages, we use the macro-pixel sampling method[23,24]; each macro-pixel is composed of N sub-pixels having a respective phase value $\phi_j = k_x\Delta x_j + k_y\Delta y_j + k_z\Delta z_j$ with $j = 1, 2, ..., N$. In each macro-pixel, the phase value ϕ_j responsible for the jth cage is randomly assigned to one of the N sub-pixels; in other words, the sub-pixel carrying ϕ_j has a different relative position with respect to the macro-pixel center for the mth and nth macro-pixels. The aperiodic arrangement of the phase value ϕ_j can avoid the periodic repetition of the entire cage array.

The left column in Fig. 5 shows a designed 3D array of multiple optical cages, distributed in two transverse planes, which are located, respectively, at $+15\lambda$ and -15λ away from the focal plane, and each of which has five cages. Figure 5(a) shows the total energy density in the transverse plane at $z = +15\lambda$. Note that the transverse plane at $z = -15\lambda$ has the same distribution as Fig. 5(a). The corresponding field intensity distributions in the longitudinal planes at $x = +15.6\lambda$ (marked by the red dashed line) and at $x = -15.6\lambda$ (marked by the white dashed line) are shown in Figs. 5(b) and 5(c), respectively. Parameters for the left panels in Fig. 5 are chosen as $\beta_0 = 1.12$, $z_d = 3\lambda$, and $t = 0.6$, which are responsible for the shape of the cage. The array-like behavior of cages is controlled by setting parameters $(\Delta x, \Delta y, \Delta z)$ in Eq. (7)

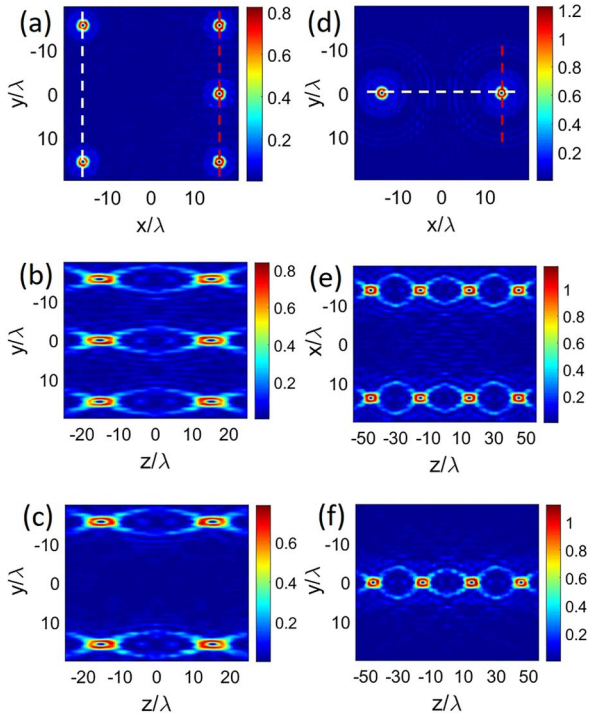

Fig. 5. Intensity distributions of multiple 3D optical cages generated in the focal volume. Left column: five cages in each of two transverse planes located, respectively, at $z = +15\lambda$ and $z = -15\lambda$; (a) intensity distribution in the transverse plane at $z = +15\lambda$, (b) intensity distribution in the longitudinal plane at $x = +15.6\lambda$, (c) intensity distribution in the longitudinal plane at $x = -15.6\lambda$. Right column: 2×1 optical cages in each of four transverse planes at $z = 45\lambda$, 15λ, -15λ, and -45λ; (d) intensity distribution in the transverse plane at $z = +15\lambda$; (e) intensity distribution in the longitudinal plane at $y = 0$; (f) intensity distribution in the longitudinal plane at $x = +13.8\lambda$.

as $\Delta x = \Delta y = \pm 15.6\lambda$, and $\Delta z = \pm 15\lambda$. The right column in Fig. 5 exhibits the total energy density of multiple 3D optical cages; four transverse planes at $z = 45\lambda, 15\lambda, -15\lambda$, and -45λ in the focal volume are assigned an array of 2×1 optical cages in each plane. Figure 5(d) presents the intensity in one of the four transverse planes ($z = +15\lambda$). The corresponding field intensity distributions in longitudinal planes at $y = 0$ [marked by the white dashed line in Fig. 5(d)] and at $x = +13.8\lambda$ (marked by the red dashed line) are shown in Figs. 5(e) and 5(f), respectively. The parameters for the right panels in Fig. 5 are chosen as $\beta_0 = 1.12$, $z_d = 3\lambda$, $t = 0.6$, $\Delta x = \pm 13.8\lambda$, $\Delta y = 0$, $\Delta z = \pm 15\lambda$, and $\Delta z = \pm 45\lambda$.

In conclusion, we have proposed a method to produce the 3D optical cage with a uniform barrier from a double-ring shaped radially and azimuthally polarized beam. The shape of the optical cage can be configured by appropriately adjusting the parameters of the double-ring-mode beam. 3D arrays of multiple optical cages are generated by applying the Fourier shifting property to the macro-pixel sampling of a double-ring shaped radially and azimuthally polarized beam. Simulation shows that the proposed principle for tailoring the structure and shape of optical cages is simple and flexible. Because the required incident beams for producing such specific focal cages can be realized by using techniques for generating a vector optical field[24], our method could facilitate applications involving vector beams, such as focus shaping and optical tweezers.

This work was supported in part by the National Natural Science Foundation of China (Nos. 91750202, 11530046, and 11474156), the National Key R&D Program of China (No. 2017YFA0303700), the Collaborative Innovation Center of Advanced Microstructures of China, and the Collaborative Innovation Center of Solid-State Lighting and Energy-Saving Electronics of China.

References

1. J. Arlt and M. J. Padgett, Opt. Lett. **25**, 191 (2000).
2. M. Neugebauer, A. Aiello, and P. Banzer, Chin. Opt. Lett. **15**, 030003 (2017).
3. L. Isenhower, W. Williams, A. Dally, and M. Saffman, Opt. Lett. **34**, 1159 (2009).
4. X. Peng, C. Chen, B. Chen, Y. Peng, M. Zhou, X. Yang, and D. Deng, Chin. Opt. Lett. **14**, 011405 (2016).
5. S. K. Mohanty, R. S. Verma, and P. K. Gupta, Appl. Phys. B **87**, 211 (2007).
6. Y. Yang, Z. Shi, J. Li, and Z. Li, Photon. Res. **4**, 2 (2016).
7. Y. Iketaki, H. Kumagai, K. Jahn, and N. Bokor, Opt. Lett. **40**, 1057 (2015).
8. R. Schmidt, C. A. Wurm, S. Jakobs, J. Engelhardt, A. Egner, and S. W. Hell, Nat. Meth. **5**, 539 (2008).
9. S. N. Khonina and I. Golub, J. Opt. Soc. Am. A **29**, 1470 (2012).
10. Y. Kozawa and S. Sato, Opt. Lett. **31**, 820 (2006).
11. Y. Chen and Y. Cai, Opt. Lett. **39**, 2549 (2014).
12. Y. Zhang, Appl. Opt. **49**, 6217 (2010).
13. N. Bokor and N. Davidson, Opt. Lett. **31**, 149 (2006).
14. X. L. Wang, J. Ding, J. Q. Qin, J. Chen, Y. X. Fan, and H. T. Wang, Opt. Commun. **282**, 3421 (2009).
15. H. Guo, X. Weng, X. Dong, G. Sui, X. Gao, and S. Zhuang, J. Opt. **40**, 206 (2011).
16. X. Weng, L. Du, P. Shi, and X. Yuan, Opt. Express **25**, 9039 (2017).
17. X. Weng, L. Du, P. Shi, and X. Yuan, Appl. Opt. **56**, 1046 (2017).
18. Q. Zhan and J. Leger, Opt. Express **10**, 324 (2002).
19. K. S. Youngworth and T. G. Brown, Opt. Express **7**, 77 (2000).
20. B. Richards and E. Wolf, Proc. R. Soc. London Ser. A **253**, 358 (1959).
21. M. Leutenegger, R. Rao, R. A. Leitgeb, and T. Lasser, Opt. Express **14**, 11277 (2006).
22. Z. Chen, T. Zeng, and J. Ding, Opt. Lett. **41**, 1929 (2016).
23. M. Yang and J. Ding, Opt. Commun. **203**, 51 (2002).
24. Z. Chen, T. Zeng, B. Qian, and J. Ding, Opt. Express **23**, 17701 (2015).